A promising non-fullerene acceptor for near-infrared organic photodetectors operating with low dark current and high response speed

Yu-Ching Huang [a,b,*], Zhi-Hao Huang [a,c], Tai-Yung Wang [a], Priyanka Chaudhary [a], Jen-Fu Hsu [d,e], Kun-Mu Lee [c,e,*]

[a] Department of Materials Engineering, Ming Chi University of Technology, New Taipei City 24301, Taiwan
[b] Organic Electronics Research Center, Ming Chi University of Technology, New Taipei City 24301, Taiwan
[c] Department of Chemical and Materials Engineering, Chang Gung University, Taoyuan 33302, Taiwan
[d] School of Medicine, College of Medicine, Chang Gung University, Taoyuan 33302 Taiwan
[e] Division of Neonatology, Department of Pediatrics, Chang Gung Memorial Hospital, Linkou, Taoyuan 33305, Taiwan

ARTICLE INFO

ABSTRACT

By tuning the band gaps of their active layer materials, organic photodetectors (OPDs) can display good responses in the near-infrared (NIR) region, making them useful for applications in biomedical imaging and optical communication. Nevertheless, NIR OPDs have tended to suffer from low specific detectivity (D*), due to a high dark current. In this study, we employed 3TT-FIC, a non-fullerene acceptor (NFA), to develop OPDs capable of operating with extremely low dark currents and high response speeds. After fine tuning the blend ratio of the donor (PM6) and acceptor (3TT-FIC), we obtained an OPD that operated at a low dark current (7.04×10^{-10} A/cm^2) at -1 V with a high value of D* (2.6×10^{13} Jones) at the wavelength of 850 nm. We also describe the wider applicability of 3TT-FIC and its good potential for applications as an NFA in NIR OPDs.

1. Introduction

Organic photodetectors (OPDs) are attractive for their tunable spectral responses, flexibility, and processability in solution at low temperature [1–3]. Recently, much research into OPDs has focused on their suitability for detectivity in the near-infrared (NIR) region (wavelengths: 780–1100 nm). Because NIR light can penetrate deeply with low scattering, it is especially suitable for optical communication [4–6], biosensing [7–9], and image sensing [1,10–12]. The primary condition for an OPD to respond in the NIR region is a donor material having a sufficiently narrow optical band gap (E_g), usually less than 1.6 eV [13,14]. The most commonly used low-band-gap donor material in organic photovoltaics (OPVs) has been poly[4,8-bis(5-(2-ethylhexyl)thien-2-yl)benzo[1,2-*b*;4,5-*b0*]-dithiophene-2,6-diyl–*alt*–(4-(2-ethylhexyl)-3-fluorothieno[3,4-*b*]-thiophene)-2-carboxylate-2,6-diyl] (PTB7-Th), which can form good bulk heterojunction (BHJ) structures with both fullerene and non-fullerene acceptor (NFA) materials. The external quantum efficiency (EQE) of devices fabricated from PTB7-Th:acceptor can be greater than 70% at NIR wavelengths (ca. 900 nm) [15–18]. Recently, NFA materials have become the main acceptor materials for

highly efficient OPVs, and the power conversion efficiency (PCE) of NFA-based OPVs has been reached 19% [19]. Among them, the most representative OPV system was based on the low-band-gap donor PM6 and the NFA Y6 demonstrated a power conversion efficiency (PCE) of greater than 15% [20,21]. An OPD fabricated from PM6:Y6 has exhibited a responsivity of 0.52 A/W at a wavelength of 850 nm [22], with rise and fall times of 1.73 and 0.97 μs, respectively. This impressive performance suggests the high applicability of PM6:Y6 systems in NIR OPDs. In addition, NFA materials have become, in the past decade, the main acceptor materials for high-efficiency OPVs, because of the possibility to tune their energy levels through molecular design. Recently, NIR OPDs incorporating various NFAs and PM6 have experienced great progress in terms of their responsivities and detection wavelengths. For example, Zhu et al. prepared an OPD based on PM6:PDTTIC-4 that displayed a record responsivity (0.55 A/W at 900 nm) and excellent shot-noise-limited specific detectivity ($D_{sh}* > 10^{13}$ Jones) [23]. McCulloch et al. synthesized O4TFIC, an ultralow-band-gap NFA, possessing a deep lowest unoccupied molecular orbital (LUMO) energy level, that absorbs light at wavelengths of up to 1020 nm; NIR OPDs based on PM6:O4TFIC displayed a maximum responsivity of 0.50 A/W

---

at 890 nm without bias voltage, performance that is comparable with silicon-based detectors [5]. In those studies, PM6 was a good donor material for NIR OPDs because of its high mobility and responsivity.

In OPDs, a low reverse dark-current density (J_d) is essential to obtaining high detectivity. A BHJ structure is commonly used for the photoactive layer, allowing facile solution processing and the formation of more donor/acceptor interfaces for efficient charge separation. Here, the intrinsic dark current results mainly from the thermal generation of charge carriers and the trap density within the BHJ photoactive layer [24]. Although Kublitski et al. studied the effect of the trap density on the dark current by tuning the donor–acceptor (D:A) ratio in the photoactive layer [25], very little related research has been performed with NIR BHJ systems. Furthermore, the reverse dark current induced by contact of the donor and acceptor with the hole transport layer (HTL) and electron transport layer (ETL) in BHJ structures can be particularly high in NIR OPD systems, because the injection barrier of the narrow-band-gap materials used in NIR OPDs is less than that of wide bandgap materials [26,27]. In particular, ZnO films with good electron transport efficiency have been extensively studied in various applications. For example, the output power of InGaN light-emitting diodes can be greatly increased by using femtosecond laser direct writing micro-holes on roughened ZnO [28]. By using ZnO nanoparticles decoration, the performance of all-inorganic $CsPbBr_3$ photodetectors can be enhanced [29]. Z. Zang et al. introduced the ZnO nanoparticles to provide an effective route for $CsPbBr_3$ nucleation, contributing a compact and smooth $CsPbBr_3$ perovskite films for enhanced random lasing [30]. They also used a low-temperature processed NH_4Cl-modified ZnO as an alternative ETL for TiO_2 to obtain a highly efficient $CsPbIBr_2$ perovskite solar cells [31]. These studies show that the ZnO layer is very suitable as an electron transport layer. Usually, the dark current of such devices having a thin active layer under a bias of –1 V is greater than 50 nA/cm^2. Therefore, decreasing the dark current of NIR OPDs will be essential to obtaining NIR OPDs displaying high detectivity. High-mobility polymers, including PNTT [32] and NT812 [33], have been used in the active layer (by increasing its thickness) to suppress the dark current without affecting the responsivity. In addition, Zhang et al. employed a charge blocking layer to decrease the dark current and improve the performance and stability [26]; they noted that the interfacial layer materials in organic solar cells and OPDs have great similarities, but not all of the former can be used in the latter. Although such methods can improve the dark currents of NIR OPDs, it remains challenging to obtain values of less than 1 nA/cm^2 under reverse bias. Thus, further research and optimization will be required to obtain extremely low dark currents for NIR OPDs.

In this paper, we demonstrate that 3TT-FIC can be used broadly as an NFA material in NIR OPDs. 3TT-FIC has previously been employed in OPVs, with power conversion efficiencies (PCEs) reaching 12% [34,35]. We applied 3TT-FIC to fabricate OPDs because its low optical energy gap (1.25 eV) allows it to absorb at wavelengths of up to 1000 nm. We blended 3TT-FIC with PM6 to form the active layers of NIR OPDs, and then evaluated the effects of its traps and morphology on the dark current the devices. By adjusting the D:A ratio in the active layer and optimizing the film thickness, we obtained NIR OPDs containing blends of PM6 and 3TT-FIC that exhibited extremely low dark currents and excellent detectivity under reverse bias. Under a bias voltage of –1 V, the dark current of the device reached as low as 0.6 nA/cm^2, with a specific detectivity in the wavelength range 400–950 nm of approximately 10^{13} Jones. The highest detectivity was at a wavelength of 850 nm (2.6 × 10^{13} Jones). In addition, the response time was less than 1 μs. To the best of our knowledge, this performance is the highest ever reported for a broadband NIR OPD. Moreover, we found that mixing PTB7-Th with 3TT-FIC also led to fairly good performance, suggesting that 3TT-FIC is indeed a very promising material for NIR OPDs.

2. Experiment

2.1. Materials

PM6, 3TT-FIC, and Y6 were purchased from 1-Material Inc.; their chemical structures are presented in Fig. 1a. Zinc acetate was obtained from Alfa Aesar. 2-Methoxylethanol, ethanolamine, chlorobenzene (CB), 1-chloronaphthalene (CN), CHCl$_3$, and MoO$_3$ were received from Sigma–Aldrich. All reagents and solvents were used without further purification.

2.2. Devices fabrication

The OPDs were fabricated on indium tin oxide (ITO)/glass substrates, which were cleaned through ultrasonication with deionized water, acetone, and isopropanol, sequentially, for 30 min. ZnO was deposited as the ETL onto the cleaned ITO substrate, and then the sample was heated at 180 °C for 30 min. ZnO was synthesized through the sol–gel method, according to a previous report [36]. PM6:3TT-FIC blends at various D:A ratios were dissolved in a mixture of chlorobenzene and CHCl$_3$ (9:1, v/v). The active layer solution comprised PM6 and Y6 (1:1.2, w/w) dissolved in CHCl$_3$ along with 0.5 vol% CN. The thicknesses of the active layers fabricated from PM6:3TT-FIC and PM6:Y6 are ~120 nm and ~100 nm, respectively. These active layer solutions were stirred at 40 °C for 12 h in a glove box. The active layer was spin-coated on the ZnO layer in a glove box, and then MoO$_3$ (5 nm, HTL) and Ag (100 nm) were deposited on the active layer through thermal evaporation. The device area was 0.04 cm^2; the band gap energy diagram is displayed in Fig. 1b.

2.3. Characterization

The film thickness was measured using an Alpha-stepper (Bruker). The dark current density–voltage (J_d–V) characteristics of the devices were recorded using a Keithley 2400 source meter. EQE spectra and responsivities at wavelengths in the range 300–1100 nm were recorded in DC mode using a QE-R system (Enlitech, Taiwan) and a silicon-based photodetector (Hamamatsu S1337), which was employed programmatically to calibrate the monochromatic beam, according to the IEC 60904-8:20146 standard. A UV–Vis spectrometer (Jasco V-750) was used to measure the absorption behavior and calculate the band gap energy of the active layer. The current density–voltage (J–V) characteristics and the noise current were recorded using a programmable source meter (Keithley, model 2636A) in the dark and under illumination from a solar simulator (Newport, 91160A) at AM 1.5G (100 mW/cm^2). The photocurrent response to the light intensity was measured through evaluation of the linear dynamic range (LDR). To measure the LDR, light-emitting diode (LED; Thorlabs, M780L2) beams (wavelength: 780 nm) were pointed at a motor-driven filter wheel (Thorlabs, FW102CNEB) to produce a controlled light intensity over the area of the OPD device. The frequency response of the OPD was measured by using a commercial LED (Thorlabs) having a luminous flux density of 1 mW/cm^2 at 850 nm, connected to a function generator (Tektronix, AFG3102C) to generate a pulse to trigger the OPD device. The output pulse of the OPD was amplified by a preamplifier operated at a low noise current with an A/V gain factor of 10^{-6}; the amplified output pulse was then captured and plotted by a 2.5 GHz oscilloscope (Teledyne LeCroy, WaveRunner 625Zi). Electrochemical impedance spectroscopy (EIS; Solartron, Materials Lab XM) was used to analyze sinusoidal AC signals in the 10^{-1} to 1 MHz sweep mode with an amplitude of 1 V. The extraction time and recombination rate of the charge carriers were obtained from transient photovoltage (TPV) and transient photocurrent (TPC) measurements, using a Paios 4.0 instrument (FLUXiM AG, Switzerland). The morphology and roughness of the film surface were measured using atomic force microscopy (AFM; Bruker). The energy loss was measured by the Fourier-transform photocurrent spectroscopy
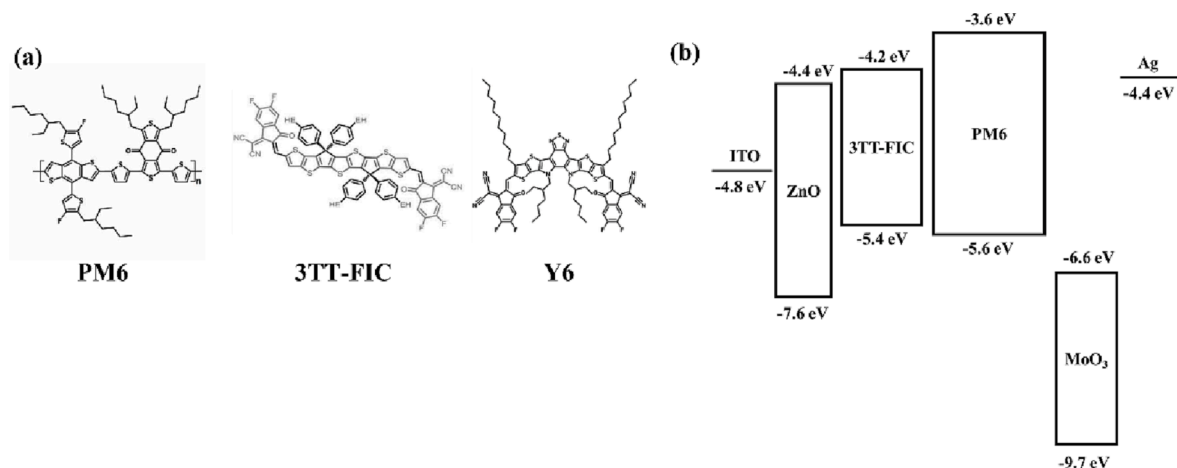
Fig. 1. (a) Chemical structures of PM6, 3TT-FIC, and Y6. (b) Band gap energy diagram of the OPD device.

external quantum efficiency (FTPS-EQE; Enlitech).

3. Results and discussion

We began this study by evaluating the effect of the D:A blend weight ratio on the dark current in the NIR region. Fig. 2a displays the UV–Vis absorption spectra of pristine samples of PM6 and 3TT-FIC. The main regions of absorption for PM6 and 3TT-FIC were 450–700 and 600–1000 nm, respectively. The complementary absorption behavior of these two materials enabled the response range of PM6:3TT-FIC blends to cover wavelengths from the visible to the NIR. To obtain OPDs capable of operating in the NIR region, the content of 3TT-FIC in the active layer was more important than the content of PM6, because the absorption of the former occurred mainly in the NIR region. Fig. 2b presents the absorption spectra of active layers containing various D:A weight ratios (0.5:2, 1:1.5, 1.5:1, and 2:0.5), with the total weight fixed at 25 mg. The un-normalized UV–Vis absorption spectra of these films are presented in Fig. S1. Upon increasing the 3TT-FIC content in the active layer, its absorption intensity in the range 700–1000 nm

increased and the signal underwent a red-shift, suggesting the enhanced crystallinity of 3TT-FIC; this enhanced crystallinity became saturated when the D:A ratio reached 1:1.5. When the content of 3TT-FIC was greater than that of PM6, the absorption intensity of PM6 decreased sharply, implying that the crystallinity of PM6 had decreased significantly. We then fabricated OPD devices according to these four D:A ratios and measured their relative performances.

Fig. 2c presents the dark current densities (J_d) of OPDs fabricated at the various D:A ratios, with the thickness of the active layer film controlled at approximately 100 nm. At a bias of −1 V, the value of J_d decreased upon increasing the PM6 content, reaching an extremely low value (ca. 6.5×10^{-10} A/cm²) at a D:A ratio of 2:0.5. This finding implies that the proportion of PM6 had a dominant effect on the dark current density under reverse bias, with better crystallinity of PM6 leading to a lower value of J_d. Notably, when the content of 3TT-FIC increased, the dark current density was first affected at a high bias voltage. When the D:A ratios were 2:0.5 and 1.5:1, the values of J_d remained low (ca. 10^{-9} A/cm²) at a high reverse bias of −3 V. When the D:A ratio reached 1:1.5, however, the dark current density at −3 V increased greatly. When the D:
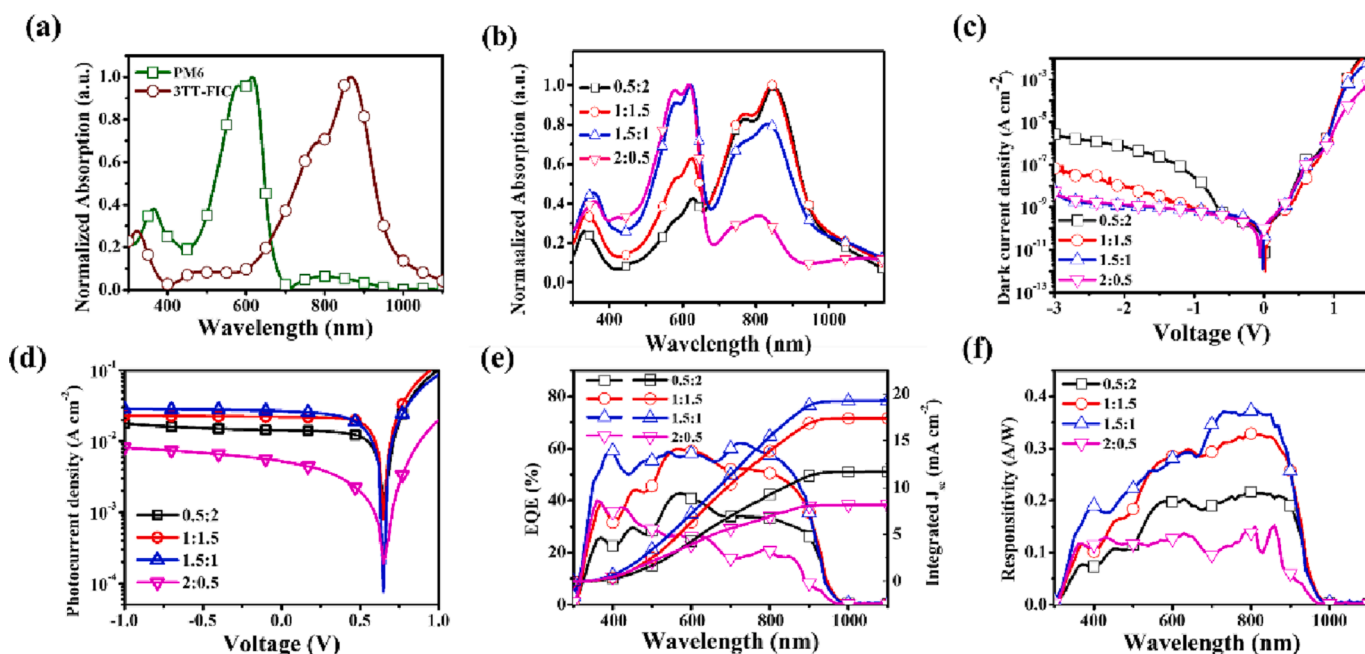

Fig. 2. (a, b) UV–Vis absorption spectra of films of (a) the pristine donor PM6 and acceptor 3TT-FIC and (b) active layers containing various D:A blend weight ratios. (c) Dark current densities, (d) photocurrent densities, (e) EQE spectra, and (f) responsivities of devices fabricated with various D:A ratios.

A ratio was 0.5:2, the value of J_d increased to 10^{-7} A/cm^2, even at –1 V. The increase in the dark current density upon increasing the 3TT-FIC content was consistent with the small injection barrier, due to the narrow-band nature of 3TT-FIC. AFM images of the surface morphologies of these devices (Fig. S2) revealed that increasing the content of 3TT-FIC led to small granular structures appearing in the deposited films, thereby increasing the surface roughness. We suspect that the small molecules of 3TT-FIC in the active layer tended to aggregate, with severe phase separation caused by excessive aggregation leading to increases in the dark current density. The low root-mean-square (RMS) surface roughness (2.53 nm) of the film fabricated at a D:A ratio of 1.5:1 indicates that it possessed few surficial defects, thereby contributing to the lower value of J_d of the corresponding device. Fig. S3 reveals the effect of the active layer thickness on the dark current density. When we decreased the active layer thickness from approximately 100 nm to approximately 60 nm, there was almost no difference in the value of J_d, suggesting that the OPDs could maintain low dark current densities even when they contained a thin active layer, thereby favoring good EQEs and detectivities.

Fig. 2d displays the photocurrent densities (J_p) of OPDs fabricated with various D:A ratios. The value of J_p decreased when the amounts of PM6 and 3TT-FIC were excessive under –1 V bias, indicating that a balanced D:A ratio was necessary for effective carrier transport. The optimal values of J_p occurred when the D:A ratios were 1.5:1 and 1:1.5. Fig. 2e presents a plot of the EQE and the simulated short-circuit photocurrent density (J_{sc}) under –1 V bias, allowing us to evaluate the degree of charge extraction. The devices prepared with active layers having D:A ratios of 0.5:2, 1:1.5, 1.5:1, and 2:0.5 provided simulated values of J_{sc} of 11.7, 17.4, 19.3, and 8.2 mA/cm^2, respectively. Thus, the device had the highest value of J_{sc} at –1 V when the D:A ratio was 1.5:1, with the EQE increasing significantly in the NIR region (700–900 nm). We calculated the responsivity of the devices according to Eq. (1): [7]

$$R = \frac{I_{ph}}{\text{light power}} = \eta_{EQE}\frac{q}{hf} = \eta_{EQE}\frac{\lambda}{1239.85}\left(\frac{A}{W}\right) \qquad (1)$$

where q is the fundamental charge (1.602×10^{-19} C), h is Planck's constant, and f is the frequency of the light source. Fig. 2f reveals that the responsivities at 850 nm of the devices fabricated with D:A ratios of 0.5:2, 1:1.5, 1.5:1, and 2:0.5 were 0.21, 0.32, 0.37, and 0.14 A/W, respectively. In addition, we calculated NIR–visible rejection ratios from the EQEs measured in the NIR (850 nm) and visible (530 nm) regions. The NIR–visible rejection ratios of the devices fabricated with D:A ratios of 0.5:2, 1:1.5, 1.5:1, and 2:0.5 were 1.35, 1.36, 1.50, and 1.26, respectively. Thus, the highest responsivity and NIR–visible rejection ratio were achieved when the D:A ratio was 1.5:1.

To investigate the excellent performance of the PM6:3TT-FIC blends, we compared them with commonly used PM6:Y6 blends. Fig. 3a presents the values of J_d of both systems. The value of J_d at –1 V bias of the device based on PM6:Y6 was 3.36×10^{-9} A/cm^2, approximately 4.8 times that of the device incorporating PM6:3TT-FIC (7.04×10^{-10} A/cm^2). When we increased the applied bias voltage to –3 V, the value of J_d of the PM6:Y6-based device was only approximately 1×10^{-6} A/cm^2, more than two orders of magnitude less than that of its PM6:3TT-FIC–based counterpart. We suspect that the potential barrier between PM6 and 3TT-FIC was larger than that of between PM6 and Y6, thereby prolonging the electron injection time and decreasing the dark current injection. Fig. 3b reveals that the responsivity of PM6:Y6 reached a maximum of 0.45 A/W at 800 nm, but, due to limited absorption, it decreased sharply for wavelengths exceeding 800 nm. In addition, the PM6:Y6 NIR–visible rejection ratio was 1.12, indicating that this system was more susceptible to visible light interference.

The noise current is one of the most important parameters of any OPD. Fig. 3c presents the noise current power spectral density (PSD), mainly composed of thermal noise, shot noise, and flicker noise, of the devices. Thermal noise is generated mainly by the thermal energy of exciton motion and the change in device resistance with respect to temperature; it is readily generated at small bias voltage. Local charge accumulation caused by many defects and grain boundaries in the active layer will also generate thermal noise currents. Shot noise arises mainly from the electronic noise generated during reverse bias operation, while
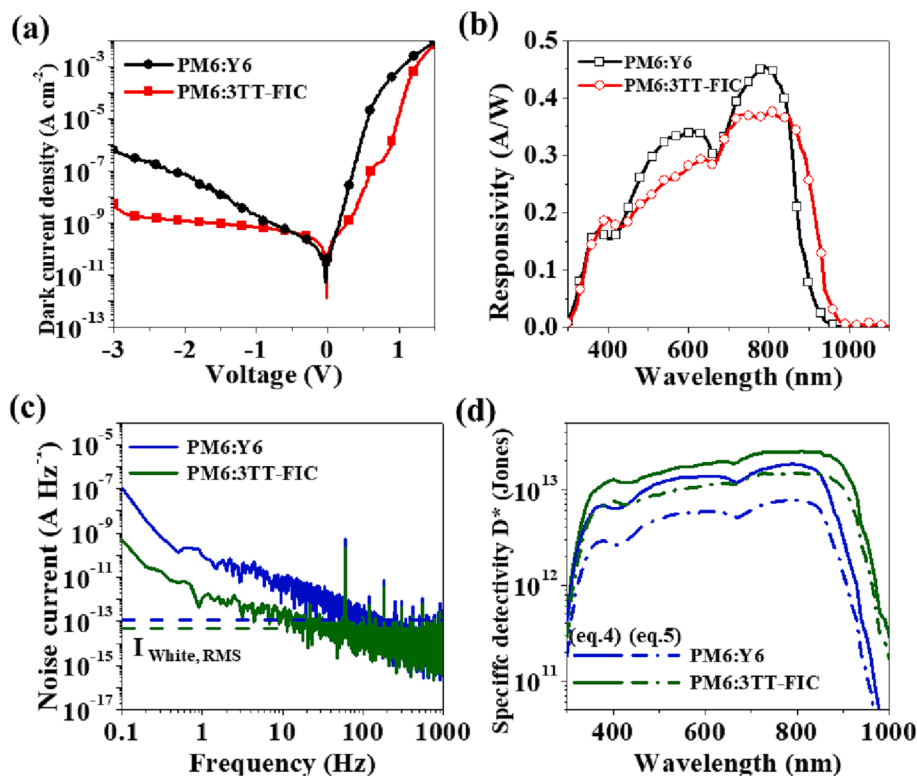

Fig. 3. (a) Dark current density, (b) responsivity, (c) noise current, and (d) specific detectivity of devices incorporating PM6:Y6 and PM6:3TT-FIC.

flicker noise (I_{fn}) is a low-frequency noise that generates its large current signal when the device is operating at low frequency. We calculated the RMS white noise ($I_{n,RMS}$) using Eq. (2): [37]

$$I_{n,RMS} = \sqrt{\int\int_{f1}^{f2} i_n^2 df} \qquad (2)$$

where the minimum (f1) and upper (f2) frequencies were set to 100 Hz and 1 kHz, respectively. In this study, we did not examine the effect of flicker noise on the component. The white noise currents at –1 V bias of the PM6:Y6– and PM6:3TT-FIC–based devices were 1.15×10^{-13} and 5.03×10^{-14} A/Hz, respectively (Table 1). Fig. S4 displays the noise currents of devices prepared at various D:A ratios at −1 V and −2 V; Table S1 lists the data.

Fig. S5 presents the effect of PM6:3TT-FIC on the various noise currents. We determined the thermal noise from the white noise current measured under zero bias (0 V) and the statistical fluctuation of the shot noise from the Eq. (3) [38]

$$I_{shot} = \sqrt{2qI_d\Delta f} \qquad (3)$$

where I_d is the dark current (A) and Δf is the noise bandwidth (Hz). The RMS thermal noise was 4.61×10^{-14} A/Hz, and the shot noise at 100 Hz was 3.03×10^{-14} A/H. Thus, the white noise of the system was dominated by the thermal noise, which might have been caused by defects in the active layer and localized charge accumulation at the grain boundaries. We obtained the shot-noise-limited specific detectivity (D^*) from the following Eq. (4), which has been used in many previous studies [39–41]:

$$D^* = R/(2qJ_d)^{1/2} \qquad (4)$$

The highest values of D^* of the devices fabricated with PM6:3TT-FIC and PM6:Y6 were 1.87×10^{13} and 1.07×10^{13} Jones, respectively, at 850 nm, as displayed by the solid lines in Fig. 3d. Notably, however, we overestimated the shot-noise-limited D^*, because the true value of D^* should also take into account the Johnson noise and flicker noise. We calculated the true value of D^* by using the Eq. (5) [40,42]

$$D^* = \frac{R\sqrt{A\Delta f}}{(i_{white,RMS})} \qquad (5)$$

where R is the responsivity (A/W), A is the illuminated area of the OPD (cm²), and $i_{white,RMS}$ is the RMS white noise. The dotted lines in Fig. 3d present the true values of D^* with respect to the noise current. The true values of D^* of the devices incorporating PM6:3TT-FIC and PM6:Y6 reached 1.45×10^{13} and 6.09×10^{12} Jones, respectively, at 850 nm under –1 V bias. We infer that both systems were dominated by thermal noise, but PM6:3TT-FIC had less effect on the thermal noise than did PM6:Y6, possibly because the higher material potential inhibited charge injection and, therefore, decreased the amount of charge accumulated in the active layer. Our findings suggest that PM6:3TT-FIC is superior to PM6:Y6 in terms of sensitivity, with excellent detectivity at 850 nm. Compared with the PM6:Y6 system, the PM6:3TT-FIC system was less affected by thermal noise, presumably because of its energy levels and

density of states (DOS) [25]. Previous literature pointed that low thermal noise in NFA blends is associated with their reduced disorder in DOS bandtails [43]. The low bandtail disorder from DOS measurement indicates that a low concentration of sub-bandgap states is occupied, which suppresses the thermal generation of carriers and enables low thermal noise current. In addition, the NFA materials with deeper energy levels resulted in the higher potential barriers, thereby reducing the generation of defects. The low concentration of thermally generated charge in the devices was generated mainly by the lowest energy state at the edge of the energy band.

We used ultraviolet photoelectron spectroscopy (UPS) to study the electronic structure of materials, using the energy distribution of the excited electrons to obtain the position of the Fermi level and the density of states in the valence band. Fig. S6 shows the kinetic and binding energies of the materials and the blends calculated by UPS spectroscopy, from which the HOMO levels can be determined. The band gap (E_g^{opt}) is then obtained from the UV–Vis absorption spectra, and the LUMO levels of the material and the blends are determined by adding E_g^{opt} to the HOMO levels. The related energy level data are listed in Table S2. Fig. 4a and 4b show the HOMO/LUMO levels of pristine materials (solid line) and blend films (dashed line) for PM6:Y6 and PM6:3TT-FIC (D:A of 1.5:1). We observed that PM6:3TT-FIC exhibited a lower LUMO level compared to that of the pristine 3TT-FIC. Normally, the LUMO level of the blend film is expected to be higher than that of the pristine material due to the intermolecular interactions after blending. However, the energy level of PM6:3TT-FIC film is shifted to a deeper position, which is favorable for capturing the minority carriers and reducing the dark current. Fig. S7 presents the characteristic values of E_{CT} of the OPDs prepared with various D:A ratios, measured using FTPS-EQE and EL calculated by fitting[43,44]. By measuring the curve of the EQE as a function of energy, the energy band structure and the charge transfer state of the materials can be inferred. The E_{CT} values of our OPDs fabricated from PM6:3TT-FIC with various D:A ratios and PM6:Y6 are listed in Table S3. The trend of E_{CT} in the PM6:3TT-FIC system is consistent with the dark current, and the Ect in PM6:Y6 system is larger than that in PM6:3TT-FIC system. To gain a more complete understanding of energy level positions in these materials, we have employed the calculation of charge-generating mid-gap (E_g^{mid}), which is a defect energy level located within the band gap of these materials. This energy level is derived by summing the LUMO level and half of the conduction band tail energy (Ect/2). For dark current, the depth of this defect level can have a significant impact on the generation of minority carriers, which are the main source of thermal noise in the device [44]. Table S3 listed the E_g^{mid} of devices fabricated from two D:A systems, and Fig. S8(a) shows that the E_g^{mid} of PM6:Y6 and PM6:3TT-FIC (D:A ratio of 1.5:1) are 4.87 eV and 4.92 eV, respectively. The deeper mid-gap state of PM6:3TT-FIC blend film is resulted from the lower LUMO and higher E_{ct}. Fig. 4c and 4d illustrate the charge-generating mid-gap of 3TT-FIC is deeper (~0.05 eV) than that of Y6, which implies a decrease in the degree of thermal charge generation. Thermal charge generation is one of the main sources of noise in organic photodetectors, and reducing the generation can improve the device performance. We further expressed the disorder of phonon states in thin films by Urbach energy (E_u) [45,46], and Fig. S8(b) illustrates the E_u and the EQE spatial disorder. The Urbach energy is determined from the slope of the tail of the absorption edge, and the E_u of PM6:Y6 and PM6:3TT-FIC are 27 meV and 25 meV, respectively. The larger E_u of PM6:Y6 indicates that the more disordered PM6:Y6, which may lead to a higher thermal noise [47]. Moreover, the thermodynamic loss $\Delta E_1 = E_g^{EQE} - E_{CT}$, depends on the formation of CT state during charge transfer process, the interfacial energetics and the morphology of active layers [43]. E_g^{EQE} is determined by the intersection of the extrapolated line of the EQE edge and the horizontal tangent line of the EQE peak, and the E_g^{EQE} and ΔE_1 of these devices are listed in Table S3. The calculated ΔE_1 of PM6:Y6 and PM6:3TT-FIC (D:A ratio of 1.5:1) are 80 meV and 50 meV, respectively. Compared to PM6:Y6, PM6:3TT-FIC exhibits a lower thermodynamic

Table 1
Performance characteristics of OPDs fabricated with PM6:Y6 and PM6:3TTFIC.

System	J_d [A/cm²][a]	EQE [%][b]	R [A/W]	$I_{white,RMS}$ [A]	D^* [Jones]
PM6:Y6	3.36×10^{-9}	52	0.35	1.15×10^{-13}	6.09×10^{12}
PM6:3TT-FIC	7.04×10^{-10}	54	0.36	5.03×10^{-14}	1.45×10^{13}

[a] Data obtained at a reverse bias voltage of –1 V.
[b] Spectra obtained from measurements at a reverse-voltage mode of –1 V with excitation at 850 nm.
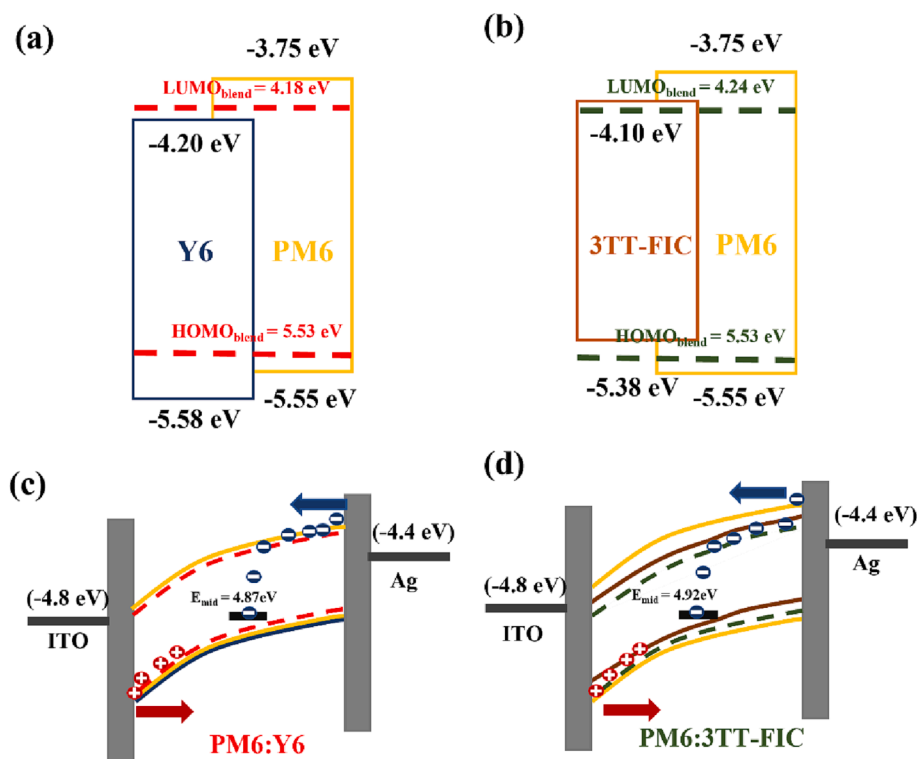
Fig. 4. Schematic representation of the (a, b) energy levels and (c, d) charge transport in PM6:Y6 (a, c) and PM6:3TT-FIC (b, d).

loss and therefore results in a low thermal noise.

We analyzed the corrected current density–voltage (J_{corr}–V_{rev}) characteristics of OPDs fabricated from various D:A ratios to better understand the charge transport behavior, as shown in Fig. S9. J_{corr} is obtained from the below Eq. (6):

$$J_{corr} = J - \frac{V_{rev} - J \times R_s}{R_{sh}} \qquad (6)$$

where J is the apparent current density, V_{rev} is the applied reverse bias, and R_s and R_{sh} are the series and shunt resistance, respectively [24,41]. As the reverse bias increases, different depletion zone widths appear on the saturated region of J_{corr}–V_{rev} curve. The slope of logarithmic J_{corr}–V_{rev} curve increases from ~1 (flat region) to over 2, representing the entry from generation current saturation zone to the space charge limited current (SCLC) zone [25,41], and the large onset voltage for the SCLC zone indicates low dark current. Fig. S10 shows that the onset voltages for the OPDs (PM6:3TT-FIC) with D:A ratios of 0.5:2, 1:1.5, 1.5:1, and 2:0.5 are 0.62, 2.38, 2.67, and 2.53 V, respectively. Compared to the onset voltage of PM6:Y6-based OPDs (1.45 V), the larger onset voltages of PM6:3TT-FIC-based OPDs indicate wider depletion zones, i. e. lower internal electric fields, preventing the charge injection through reverse bias. In addition, the PM6:3TT-FIC–based device prepared with the D:A ratio of 1.5:1 has the largest R_{sh} (4.58×10^9 Ω cm^2) in comparison to that of the PM6:Y6-based OPDs (3.56×10^8 Ω cm^2), as shown in Table S4. These results demonstrate that the extremely low dark current of the PM6:3TT-FIC-based OPDs is caused by the reduced shunt leakage and wide depletion zone.

We evaluate the carrier mobilities of these blend films the by space-charge-limited current (SCLC) method, as shown in Fig. S10(d) and listed in Table S4. The blend film with D:A ratio of 1.5:1 exhibits the highest hole mobility (μ_h) and electron mobility (μ_e) of 2.7×10^{-4} and 2.2×10^{-4} cm^{2}V^{-1}S^{-1}, respectively; the relatively balanced μ_h and μ_e also imply a small built-in electric field and low non-radiative loss. Low drak current results from limited charge recombination [48]. Moreover, we calculated the trap filling voltage (V_{TFL}) and electron defect density (N_t)

by using the equation of $V_{TFL} = (qN_t L^2)/ 2\varepsilon\varepsilon_0$, where q is the fundamental charge, L is the film thickness, ε and ε_0 are the dielectric constant and vacuum dielectric constant, respectively. Fig. S11 shows that the OPD with D:A ratio of 1.5:1 has the lowest V_{TFL} value of 0.57 V and the minimum N_t value of 2.98×10^{15} cm^{-3}, indicating the reduced defects in the blend film. These results also provide evidences for the low J_d of the PM6:3TT-FIC-based OPDs under reverse bias. For better understand the influence of the blending ratio of the device on the performance, we further conducted the transient photocurrent (TPC) and transient photovoltage (TPV) measurements to examine the charge carrier behaviors of OPDs fabricated from PM6:3TT-FIC with various D:A ratios shown in Fig. S12. TPC and TPV were used to evaluate charge extraction time and carrier lifetime of the devices, as listed in Table S5. The OPDs fabricated from D:A ratio of 1.5:1 exhibit the fastest TPC decay time (0.81 μs) and the slowest TPV decay time (86 μs), indicating the best charge extraction efficiency and longest carrier lifetime of the devices, respectively. Combined with the morphologies obtained by AFM, the TPC and TPV results elucidate the effect of film roughness on charge extraction and recombination.

To determine the response speed capabilities of the devices for practical applications, we measured their frequency responses at –2 V. We obtained the response speed of the OPDs from the –3 dB cutoff frequency ($f_{-3 \, dB}$) and the response time. The value of $f_{-3 \, dB}$ was the frequency of the modulated light at which the photocurrent decreased to $1/\sqrt{2}$ of the initial photocurrent measured under continuous illumination. Fig. 5a presents the cutoff frequencies of the PM6:3TT-FIC and PM6:Y6 systems. The PM6:3TT-FIC–based device prepared with a D:A ratio of 1.5:1 exhibited the best $f_{-3 \, dB}$ with a maximum width of approximately 550 kHz. To investigate the origin of the fast response rate, we divided the value of $f_{-3 \, dB}$ into two parts: the RC circuit response and the photogenerated charge carriers, where the RC circuit includes series resistance (R_s) and capacitance (C). Fig. S13(a) displays the Nyquist plot measured using EIS; the series resistance of the PM6:3TT-FIC blend was larger than that of the PM6:Y6 blend. The EIS spectra and corresponding Nyquist plots were fitted to calculate the circuit components R_S, R_{CT}, and C_{DL}, where R_{CT} is the charge transfer resistance (Ω) and C_{DL} is the
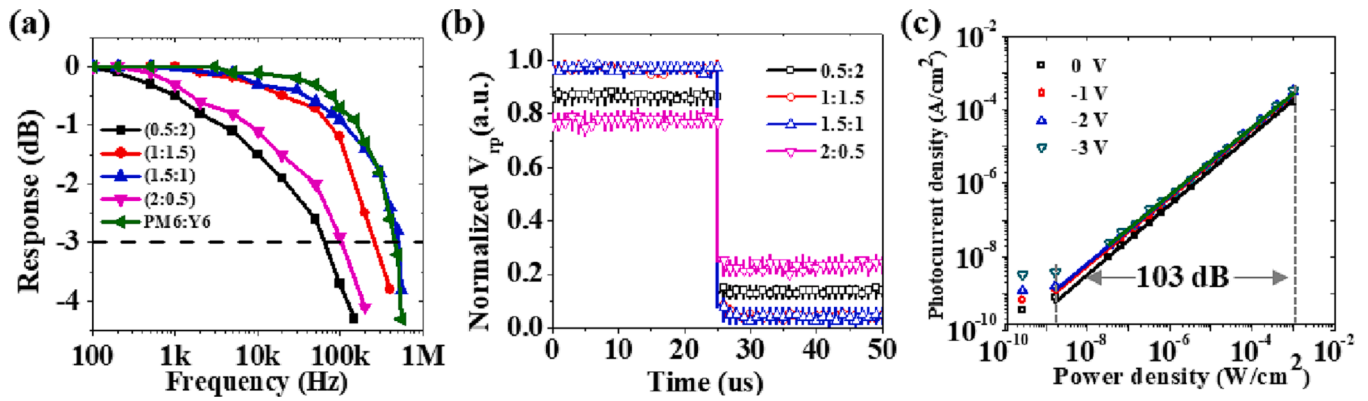
Fig. 5. (a) Cutoff frequencies of the PM6:3TT-FIC and PM6:Y6 systems. (b) Response times of devices incorporating PM6:3TT-FIC at various D:A ratios at –2 V bias. (c) LDRs of PM6:3TT-FIC–based devices operated at various biases.

double-layer capacitance (F). Accordingly, we obtained the RC-based frequency response ($f_{RC-3\ dB}$) by using the following equation with $R = R_s$ and $C = C_{DL}$ [44]:

$$f_{RC,-3dB} = \frac{1}{2\pi R_S C} \tag{7}$$

These data are similar to the values of $f_{-3\ dB}$ obtained from the oscilloscope measurements. In addition, Fig. S13(b) shows the capacitance versus frequency measurement of these OPDs. The NFA materials with deeper energy levels resulted in the higher potential barriers, thereby reducing the generation of defects. The defect state density can be calculated from the capacitance versus frequency measurement, and the number of traps is proportional to the capacitance [25,49]. We can observe that the PM6:3TT-FIC exhibits lower capacitance, indicating better trap inhibition. Fig. 5b presents the response times of the devices incorporating PM6:3TT-FIC with various D:A ratios at –2 V bias; the best device exhibited rise and fall times of approximately 0.7 and 0.8 μs, respectively. A high response rate could be obtained for a thin active layer, high carrier mobility, and suppressed RC time. We calculated the hysteresis time constant τ according to the equation [41,50]

$$\tau = R_{CT} C_{DL} \tag{8}$$

here, the value of τ is related to the discharge rate of the OPDs. For the PM6:Y6 system, the value of τ was 8.3 ms; for the PM6:3TT-FIC devices with D:A ratios of 0.5:2, 1:1.5, 1.5:1, and 2:0.5, the values were 5.0, 9.9, 10.1, and 18.4 ms, respectively. PM6 has a large potential to increase the time of electron injection and, therefore, has a very fast discharge rate in the dark, effectively inhibiting the rise in dark current under a bias voltage. In addition, the actual response speeds measured from the TPC data were 6.82 ns for the PM6:Y6 system and 10.64, 5.6, 5.16, and 5.39 ns for the PM6:Y6 systems with D:A ratios of 0.5:2, 1:1.5, 1.5:1, and 2:0.5, respectively. We measured the LDRs of the PM6:3TT-FIC–based devices by using 780-nm LEDs and employing reverse biases from 0 to –3 V Fig. 5c. We calculated the LDRs using the equation [51].

$$LDR = 20\log\frac{J_{ph}}{J_d} \tag{9}$$

The LDRs for the PM6:Y6 systems with D:A ratios of 0.5:2, 1:1.5, 1.5:1, and 2:0.5 were 106, 107, 106, and 82 dB, respectively. The feasibility of using PM6:3TT-FIC blends for NIR detection was indicated by the effective suppression of dark current injection at a bias voltage of –2 V and the maintenance of the LDR.

To demonstrate the broader applicability of 3TT-FIC as a promising NIR acceptor material, we fabricated NIR OPDs containing a blend of PTB7-Th and 3TT-FIC. Fig. S14 reveals that the OPD devices based on PTB7-Th:3TT-FIC exhibited values of J_d of 8.36 × 10^{-9} A/cm^2 at –1 V and 2.84 × 10^{-8} A/cm^2 at –3 V. The responsivity of the OPDs at 850 nm

was 0.45 A/W, with a detectivity of 8.70 × 10^{12} Jones calculated from the value of J_d and the responsivity. In addition, the LDR was 103 dB at –1 V, with a cutoff frequency of 300 kHz. The rise and fall times of the OPDs based on PTB7-Th:3TT-FIC (1.6 and 1.2 μs, respectively). In addition to the broader applicability, 3TT-FIC also exhibits better operating lifetime and process yield. Previous studies have reported that the PM6:Y6 system is prone to photo-degradation in the ambient environment [52], implying that the OPDs fabricated from Y6 acceptor materials perform poorly in ambient condition. We compared the J_d and EQE of OPDs fabricated from PM6:Y6 and PM6:3TT-FIC under N$_2$ and ambient conditions, and the results are shown in Fig. S15a and S15b. Compared with Y6-based OPDs, the J_d values of 3TT-FIC-based OPDs are almost the same under N$_2$ and ambient conditions, implying that 3TT-FIC acceptor material has great potential for low-cost commercialization. Fig. S15c shows the unchanged J_d and EQE values of 3TT-FIC-based unencapsulated devices after dark storage in a dry box (~40% relative humidity) for 180 h. However, the J_d of Y6-based devices was increased by about 40 times, which indicated that the 3TT-FIC exhibits excellent stability. Moreover, Fig. S15d illustrates the J_d variation for 20 devices fabricated from PM6:Y6 and PM6:3TT-FIC, respectively. The PM6:3TT-FIC-based OPDs exhibits a small J_d variation, indicating a better process yield in comparison with PM6:Y6-based OPDs. Table S5 summarizes the performance of state-of-the-art NIR OPDs at similar wavelengths. Our OPDs featuring 3TT-FIC as the acceptor displayed promising performance, especially in terms of their nanoampere-level dark current densities and sub-microsecond response times in the NIR.

4. Conclusion

We have investigated the effect of the D:A ratio of PM6:3TT-FIC blends on the dark current density and photodetection performance of NIR OPDs. In comparison with the commonly used NFA Y6, the values of J_d of OPDs incorporating 3TT-FIC as the NFA (mixed with PM6 as the donor) were extremely low (ca. 10^{-10} A/cm^2), and they could remain low even at a high reverse bias voltage (–3 V). This behavior was due to the energy band alignment of 3TT-FIC and PM6 effectively decreasing the value of J_d that resulted from the low LUMO energy level. In addition, there was no need to increase the thickness of the active layer to decrease the dark current when using 3TT-FIC, with the thinner active layer film leading to good EQE and charge transport behavior. As a result, we achieved an OPD incorporating PM6:3TT-FIC that displayed a high value of D^* in the NIR region and sub-microsecond response times. Furthermore, we could also blend 3TT-FIC with other polymers to obtain NIR OPDs displaying comparable performance. We hope that this study will help to pave the way toward the preparation of high-performance NIR OPDs.

Declaration of Competing Interest

The authors declare that they have no known competing financial interests or personal relationships that could have appeared to influence the work reported in this paper.

Data availability

Data will be made available on request.

Acknowledgements

Appendix A. Supplementary data

Supplementary data to this article can be found online at https://doi.org/10.1016/j.cej.2023.142633.

References

[1] Z. Zhao, C. Xu, L. Niu, X. Zhang, F. Zhang, Recent progress on broadband organic photodetectors and their applications, Laser Photonics Rev. 14 (2020) 2000262.

[2] D. Yang, D. Ma, Development of organic semiconductor photodetectors: from mechanism to applications, Adv. Opt. Mater. 7 (2019) 1800522.

[3] P.C.Y. Chow, T. Someya, Organic photodetectors for next-generation wearable electronics, Adv. Mater. 32 (2020) 1902045.

[4] J. Liu, J. Jiang, S. Wang, T. Li, X. Jing, Y. Liu, Y. Wang, H. Wen, M. Yao, X. Zhan, L. Shen, Fast response organic tandem photodetector for visible and near-infrared digital optical communications, Small 17 (2021) 2101316.

[5] M. Babics, H. Bristow, W. Zhang, A. Wadsworth, M. Neophytou, N. Gasparini, I. McCulloch, Non-fullerene-based organic photodetectors for infrared communication, J. Mater. Chem. C 9 (7) (2021) 2375–2380.

[6] W. Li, S. Li, L. Duan, H. Chen, L. Wang, G. Dong, Z. Xu, Squarylium and rubrene based filterless narrowband photodetectors for an all-organic two-channel visible light communication system, Org. Electron. 37 (2016) 346–351.

[7] R.D. Jansen-van Vuuren, A. Armin, A.K. Pandey, P.L. Burn, P. Meredith, Organic photodiodes: the future of full color detection and image sensing, Adv. Mater. 28 (2016) 4766–4802.

[8] J. Qi, W. Qiao, Z.Y. Wang, Advances in organic near-infrared materials and emerging applications, Chem. Rec. 16 (3) (2016) 1531–1548.

[9] T. Yokota, T. Nakamura, H. Kato, M. Mochizuki, M. Tada, M. Uchida, S. Lee, M. Koizumi, W. Yukita, A. Takimoto, T. Someya, A conformable imager for biometric authentication and vital sign measurement, Nat. Electr. 3 (2020) 113–121.

[10] M. Biele, C. Montenegro Benavides, J. Hürdler, S.F. Tedde, C.J. Brabec, O. Schmidt, Spray-coated organic photodetectors and image sensors with silicon-like performance, Adv. Mater. Technol. 4 (2019) 1800158.

[11] M.G. Han, K.-B. Park, X. Bulliard, G.H. Lee, S. Yun, D.-S. Leem, C.-J. Heo, T. Yagi, R. Sakurai, T. Ro, S.-J. Lim, S. Sul, K. Na, J. Ahn, Y.W. Jin, S. Lee, Narrow-band organic photodiodes for high-resolution imaging, ACS Appl. Mater. Interfaces 8 (39) (2016) 26143–26151.

[12] G. Simone, M.J. Dyson, S.C.J. Meskers, R.A.J. Janssen, G.H. Gelinck, Organic photodetectors and their application in large area and flexible image sensors: the role of dark current, Adv. Funct. Mater. 30 (20) (2020) 1904205.

[13] J. Liu, M. Gao, J. Kim, Z. Zhou, D.S. Chung, H. Yin, L. Ye, Challenges and recent advances in photodiodes-based organic photodetectors, Mater. Today 51 (2021) 475–503.

[14] J. Liu, Y. Wang, H. Wen, Q. Bao, L. Shen, L. Ding, Organic photodetectors: materials, structures, and challenges, Solar RRL 4 (2020) 2000139.

[15] X. Gao, H. Wang, Z. Li, X. Tao, X. Qin, T. Yang, X. Song, L. Bu, G. Lu, Y. Tao, Contrastive manipulations on vertical stratifications by a fluorescent guest component in ternary nonfullerene and fullerene organic solar cells, Chem. Eng. J. 450 (2022) 138018.

[16] X. Liao, H. Pei, H. Zhao, Y. Cui, L. Li, X. Shi, P. Zhu, W. Ma, Y. Chen, A.K.Y. Jen, The synergistic effects of central core size and end group engineering on performance of narrow bandgap nonfullerene acceptors, Chem. Eng. J. 435 (2022), 135020.

[17] X. Kong, H. Lin, X. Du, L. Li, X. Li, X. Chen, C. Zheng, D. Wang, S. Tao, Hydrogen bond induced high performance ternary fullerene-free organic solar cells with increased current density and enhanced stability, J. Mater. Chem. C 6 (36) (2018) 9691–9702.

[18] C. Li, Q. Yue, H. Wu, B. Li, H. Fan, X. Zhu, Small bandgap non-fullerene acceptor enables efficient PTB7-Th solar cell with near 0 eV HOMO offset, J. Energy Chem. 52 (2021) 60–66.

[19] D. Li, N. Deng, Y. Fu, C. Guo, B. Zhou, L. Wang, J. Zhou, D. Liu, W. Li, K. Wang, Y. Sun, T. Wang, Fibrillization of non-fullerene acceptors enables 19% efficiency pseudo-bulk heterojunction organic solar cells, Adv. Mater. 35 (6) (2023) 2208211.

[20] J. Yuan, Y. Zhang, L. Zhou, G. Zhang, H.-L. Yip, T.-K. Lau, X. Lu, C. Zhu, H. Peng, P. A. Johnson, M. Leclerc, Y. Cao, J. Ulanski, Y. Li, Y. Zou, Single-junction organic solar cell with over 15% efficiency using fused-ring acceptor with electron-deficient core, Joule 3 (4) (2019) 1140–1151.

[21] M. Deng, H. Meng, X. Xu, J. Tang, L. Yu, R. Li, Q. Peng, Unique W-Shape Y6 isomer as effective solid additive for High-Performance PM6:Y6 polymer solar cells, Chem. Eng. J. 440 (2022), 135975.

[22] Y. Zhang, Z. Qin, X. Huo, D. Song, B. Qiao, S. Zhao, High-performance near-infrared photodetectors based on the synergy effect of short wavelength light filter and long wavelength response of a perovskite/polymer hybrid structure, ACS Appl. Mater. Interfaces 13 (51) (2021) 61818–61826.

[23] Y. Chen, Y. Zheng, Y. Jiang, H. Fan, X. Zhu, Carbon-bridged 1,2-bis(2-thienyl) ethylene: an extremely electron rich dithiophene building block enabling electron acceptors with absorption above 1000 nm for highly sensitive nir photodetectors, J. Am. Chem. Soc. 143 (2021) 4281–4289.

[24] G. Simone, M.J. Dyson, C.H.L. Weijtens, S.C.J. Meskers, R. Coehoorn, R.A. J. Janssen, G.H. Gelinck, On the origin of dark current in organic photodiodes, Adv. Opt. Mater. 8 (2020) 1901568.

[25] J. Kublitski, A. Hofacker, B.K. Boroujeni, J. Benduhn, V.C. Nikolis, C. Kaiser, D. Spoltore, H. Kleemann, A. Fischer, F. Ellinger, K. Vandewal, K. Leo, Reverse dark current in organic photodetectors and the major role of traps as source of noise, Nat Commun 12 (2021) 551.

[26] Y. Li, H. Chen, J. Zhang, Carrier blocking layer materials and application in organic photodetectors, Nanomaterials 11 (2021) 1404.

[27] Z. Zhong, Z. Zeng, Z. Huang, F. Peng, P. He, L. Lan, L. Ying, Effects of charge injection barrier on the dark current of organic photodiodes, Org. Electron. 109 (2022), 106621.

[28] Z. Zang, X. Zeng, J. Du, M. Wang, X. Tang, Femtosecond laser direct writing of microholes on roughened ZnO for output power enhancement of InGaN light-emitting diodes, Opt. Lett. 41 (2016) 3463–3466.

[29] C. Li, C. Han, Y. Zhang, Z. Zang, M. Wang, X. Tang, J. Du, Enhanced photoresponse of self-powered perovskite photodetector based on ZnO nanoparticles decorated CsPbBr 3 films, Sol. Energy Mater. Sol. Cells 172 (2017) 341–346.

[30] C. Li, Z. Zang, C. Han, Z. Hu, X. Tang, J. Du, Y. Leng, K. Sun, Highly compact CsPbBr 3 perovskite thin films decorated by ZnO nanoparticles for enhanced random lasing, Nano Energy 40 (2017) 195–202.

[31] H. Wang, S. Cao, B. Yang, H. Li, M. Wang, X. Hu, K. Sun, Z. Zang, NH4Cl-modified ZnO for high-performance CsPbIBr 2 perovskite solar cells via low-temperature process, Solar RRL 4 (2020) 1900363.

[32] Z. Zeng, Z. Zhong, W. Zhong, J. Zhang, L. Ying, G. Yu, F. Huang, Y. Cao, High-detectivity organic photodetectors based on a thick-film photoactive layer using a conjugated polymer containing a naphtho[1,2-c:5,6-c]bis[1,2,5]thiadiazole unit, J. Mater. Chem. C 7 (20) (2019) 6070–6076.

[33] B. Xie, R. Xie, K. Zhang, Q. Yin, Z. Hu, G. Yu, F. Huang, Y. Cao, Self-filtering narrowband high performance organic photodetectors enabled by manipulating localized Frenkel exciton dissociation, Nat. Commun. 11 (2020) 2871.

[34] Y. Li, J.-D. Lin, X. Liu, Y. Qu, F.-P. Wu, F. Liu, Z.-Q. Jiang, S.R. Forrest, Near-infrared ternary tandem solar cells, Adv. Mater. 30 (2018) 1804416.

[35] H.-H. Gao, Y. Sun, X. Wan, X. Ke, H. Feng, B. Kan, Y. Wang, Y. Zhang, C. Li, Y. Chen, A new nonfullerene acceptor with near infrared absorption for high performance ternary-blend organic solar cells with efficiency over 13%, Adv. Sci. 5 (2018) 1800307.

[36] Y.-M. Sung, A.K. Akbar, S. Biring, C.-F. Li, Y.-C. Huang, S.-W. Liu, The effect of ZnO preparation on the performance of inverted polymer solar cells under one sun and indoor light, J. Mater. Chem. C 9 (4) (2021) 1196–1204.

[37] C. Fuentes-Hernandez, W.-F. Chou, T.M. Khan, L. Diniz, J. Lukens, F.A. Larrain, V. A. Rodriguez-Toro, B. Kippelen, Large-area low-noise flexible organic photodiodes for detecting faint visible light, Science 370 (6517) (2020) 698–701.

[38] Z. Lan, Y. Lei, W.K.E. Chan, S. Chen, D. Luo, F. Zhu, Near-infrared and visible light dual-mode organic photodetectors, Sci. Adv. 6 (5) (2020).

[39] Y.-L. Wu, K. Fukuda, T. Yokota, T. Someya, A highly responsive organic image sensor based on a two-terminal organic photodetector with photomultiplication, Adv. Mater. 31 (2019) 1903687.

[40] J.-H. Lu, B.-H. Jiang, F.-C. Hsiao, Y.-C. Peng, Y.-W. Su, Y.-R. Lin, T.-H. Tsai, M.-N. Shiu, C.-Y. Lin, Y.-T. Fang, C.-P. Chen, High-performance organic photodiodes for blue-light hazard detection, Chem. Eng. J. 437 (2022), 135327.

[41] J. Huang, J. Lee, J. Vollbrecht, V.V. Brus, A.L. Dixon, D.X. Cao, Z. Zhu, Z. Du, H. Wang, K. Cho, G.C. Bazan, T.-Q. Nguyen, A high-performance solution-processed organic photodetector for near-infrared sensing, Adv. Mater. 32 (1) (2020) 1906027.

[42] M.Y. Hadiyanto, R. Estrada, C.-C. Lee, S. Biring, A.K. Akbar, C.-Y. Li, C.-J. Shih, Y.-Z. Li, S.-W. Liu, Transparent photodetectors with ultra-low dark current and high photoresponse for near-infrared detection, Org. Electron. 99 (2021), 106356.

[43] Z. Xing, X. Meng, R. Sun, T. Hu, Z. Huang, J. Min, X. Hu, Y. Chen, An effective method for recovering nonradiative recombination loss in scalable organic solar cells, Adv. Funct. Mater. 30 (2020) 2000417.

[44] N. Zarrabi, O.J. Sandberg, S. Zeiske, W. Li, D.B. Riley, P. Meredith, A. Armin, Charge-generating mid-gap trap states define the thermodynamic limit of organic photovoltaic devices, Nat. Commun. 11 (2020) 5567.

[45] L. Perdigón-Toro, L.Q. Phuong, F. Eller, G. Freycht, E. Saglamkaya, J.I. Khan, Q. Wei, S. Zeiske, D. Kroh, S. Wedler, A. Köhler, A. Armin, F. Laquai, E.M. Herzig, Y. Zou, S. Shoaee, D. Neher, Understanding the role of order in Y-series non-fullerene solar cells to realize high open-circuit voltages, Adv. Energy Mater. 12 (2022) 2103422.

[46] N. Jain, N. Chandrasekaran, A. Sadhanala, R.H. Friend, C.R. McNeill, D. Kabra, Interfacial disorder in efficient polymer solar cells: the impact of donor molecular structure and solvent additives, J. Mater. Chem. A 5 (2017) 24749–24757.

[47] C. Kaiser, O.J. Sandberg, N. Zarrabi, W. Li, P. Meredith, A. Armin, A universal Urbach rule for disordered organic semiconductors, Nat. Commun. 12 (2021) 3988.

[48] P. Kafourou, Z. Qiao, M. Tóth, F. Aniés, F. Eisner, N. Gasparini, M. Heeney, Low dark current organic photodetectors utilizing highly cyanated non-fullerene acceptors, ACS Appl. Mater. Interfaces 14 (34) (2022) 39141–39148.

[49] Z. Wu, N. Li, N. Eedugurala, J.D. Azoulay, D.-S. Leem, T.N. Ng, Noise and detectivity limits in organic shortwave infrared photodiodes with low disorder, npj Flexible, Electronics 3 (2020) 100711.

[50] C.-C. Lee, R. Estrada, Y.-Z. Li, S. Biring, N.R.A. Amin, M.-Z. Li, S.-W. Liu, K.-T. Wong, Vacuum-processed small molecule organic photodetectors with low dark current density and strong response to near-infrared wavelength, Adv. Opt. Mater. 8 (2020) 2000519.

[51] M. Kielar, O. Dhez, G. Pecastaings, A. Curutchet, L. Hirsch, Long-term stable organic photodetectors with ultra low dark currents for high detectivity applications, Sci. Rep. 6 (2016) 39201.

[52] Y. Han, H. Dong, W. Pan, B. Liu, X. Chen, R. Huang, Z. Li, F. Li, Q. Luo, J. Zhang, Z. Wei, C.Q. Ma, An efficiency of 16.46% and a T(80) lifetime of over 4000 h for the PM6:Y6 inverted organic solar cells enabled by surface acid treatment of the zinc oxide electron transporting layer, ACS Appl. Mater. Interfaces 13 (2021) 17869–17881.